Avik Samanta
Department of Mechanical and Industrial Engineering,
University of Iowa,
Iowa City, IA 52242

Ninggang Shen
Department of Mechanical and Industrial Engineering,
University of Iowa,
Iowa City, IA 52242

Haipeng Ji
Department of Mechanical and Industrial Engineering,
University of Iowa,
Iowa City, IA 52242;
Research Institute for Energy Equipment Materials,
Hebei University of Technology,
Tianjin 300130, China

Weiming Wang
Department of Mechanical Engineering,
University of Hawaii at Manoa,
Honolulu, HI 96822

Jingjing Li
The Harold and Inge Marcus Department of Industrial and Manufacturing Engineering,
Penn State University,
State College, PA 16801

Hongtao Ding[1]
Department of Mechanical and Industrial Engineering,
University of Iowa,
Iowa City, IA 52242
e-mail: hongtao-ding@uiowa.edu

Cellular Automaton Simulation of Microstructure Evolution for Friction Stir Blind Riveting

Friction stir blind riveting (FSBR) process offers the ability to create highly efficient joints for lightweight metal alloys. During the process, a distinctive gradient microstructure can be generated for the work material near the rivet hole surface due to high-gradient plastic deformation and friction. In this work, discontinuous dynamic recrystallization (dDRX) is found to be the major recrystallization mechanism of aluminum alloy 6111 undergoing FSBR. A cellular automaton (CA) model is developed for the first time to simulate the evolution of microstructure of workpiece material during the dynamic FSBR process by incorporating main microstructure evolution mechanisms, including dislocation dynamics during severe plastic deformation, dynamic recovery, dDRX, and subsequent grain growth. Complex thermomechanical loading conditions during FSBR are obtained using a mesh-free Lagrangian particle-based smooth particle hydrodynamics (SPH) method, and are applied in the CA model to predict the microstructure evolution near the rivet hole. The simulation results in grain structure agree well with the experiments, which indicates that the important characteristics of microstructure evolution during the FSBR process are well captured by the CA model. This study presents a novel numerical approach to model and simulate microstructure evolution undergoing severe plastic deformation processes. [DOI: 10.1115/1.4038576]

Keywords: cellular automaton, friction stir blind riveting, microstructure evolution, discontinuous dynamic recrystallization, aluminum alloy

1 Introduction

Friction stir blind riveting (FSBR) process was developed by combining friction stir and blind riveting processes for joining light sheet metals [1,2]. During the process, a high-speed rotating (typically 2000–12,000 rpm) blind rivet is brought in contact with the topmost sheet of a stack of sheet metals. The work materials get softened due to the heat generated during frictional interaction between rivet and workpiece leading to a reduction of required force to drive the rivet into the workpieces. When the rivet is fully inserted into the workpieces, it is upset as in conventional blind riveting. Multilayer multiple materials can be joined at a high speed using this method in lap joint configuration.

The FSBR process and joint performance have been experimentally investigated for similar and dissimilar materials. Gao et al. [2] conducted an experimental analysis of the FSBR process on aluminum alloy 5052. Their study demonstrated that FSBR can provide higher static and fatigue strengths compared with the resistance spot welding process. Min et al. [3,4] evaluated the effects of process parameters of the FSBR process and reported that both increase in spindle speed and decrease in feed rate reduce the required penetration force during FSBR. More thermal softening took place at the higher rotational interaction between the rivet mandrel and workpiece material. Lathabai et al. [5] found that a hollow mandrel head design also reduces penetration force and eliminates burr formation during the process, thus providing a guideline for rivet design for the FSBR process. The FSBR process has also been investigated to join dissimilar materials, such as magnesium and aluminum alloys [5–7], which are very difficult to weld together otherwise. These prior research findings showed that placement of the sheets played a significant role in joint strength, and the material around the rivet shank got hardened during the penetration process. In addition, Min et al. [8] also demonstrated that the FSBR process can be used for joining carbon-fiber reinforced polymer composites to aluminum alloy and the joint strength also relies on the track-up sequence of work materials.

Significant microstructural alterations have been experimentally observed and analyzed for friction stir-based processes, especially friction stir welding, for various engineering alloys such as aluminum alloys [9–12], magnesium alloys [13,14], steels [15,16] and dissimilar materials [17–19]. Fundamental understanding of microstructure evolution mechanisms is essential for prediction and control of the mechanical properties of the end product from these friction stir processes, which often involves complex dynamic thermomechanical loading conditions dominated by high-speed rotation, strong friction at the tool–workpiece

[1]Corresponding author.

Manuscript received October 9, 2017; final manuscript received November 17, 2017; published online January 3, 2018. Assoc. Editor: Wayne Cai.

interface, and severe plastic deformation. Prior research has identified dynamic recrystallization (DRX) as a major microstructure evolution mechanism during friction stir processes [9–12,14,16]. It has been experimentally observed that a refined gradient microstructure was a result of DRX from the FSBR process [20]. Some finite element modeling (FEM) efforts with Zener–Hollomon parameter-based empirical material models have been developed to model DRX during other severe plastic deformation processes such as metal cutting [21,22]. However, these models were unable to capture the dynamic process characteristics of microstructure evolution during FSBR.

Cellular automaton (CA) has provided the capability to simulate and predict the evolution of microstructure during metal forming processes [23–26]. In particular, CA methods have been developed to simulate the microstructure evolution governed by DRX during hot forming processes of various metals such as steels [23,27–33], copper [24,25,34–37], magnesium alloys [26,38,39], and titanium alloy [40,41]. These previous works demonstrated that the CA method is a computation-efficient numerical approach to simulate microstructure evolution. However, these previous works focused on processes with low strain rates and usually under constant thermal loadings. According to the authors' best knowledge, few numerical modeling efforts can be found in literature to simulate microstructure evolution during the FSBR process. The complex coupling interactions between severe plastic deformation, thermal field, and microstructure evolution made it difficult to model microstructure change in friction stir processes.

In this work, a comprehensive analysis of microstructure evolution mechanisms is discussed for the FSBR process of aluminum alloy AA6111-T4. A two-dimensional CA model is developed for the first time to simulate the evolution of material microstructure in the FSBR process by incorporating main microstructure evolution mechanisms including dislocation dynamics during severe plastic deformation, dynamic recovery, discontinuous dynamic recrystallization (dDRX), and subsequent grain growth. Complex thermomechanical loading conditions during FSBR are obtained using a mesh-free Lagrangian particle-based smooth particle hydrodynamics (SPH) method, and are applied in the CA model to simulate the microstructure evolution near the rivet hole.

2 Principle of Microstructural Evolution During FSBR

2.1 Microstructural Analysis. The microstructural analysis conducted in this work is based on a previously published experimental study by Min et al. [20]. Table 1 lists the conditions for FSBR experiments, which used blind rivets (SSPV-08-06 by Advel®) with a shank diameter 6.4 mm. The rivets were made of mild steel and had a fine zinc coating on the surface. During the experiments, a single layer of 0.9 mm thick AA6111-T4 work material was investigated for the FSBR process.

The work material AA6111-T4 sheet was rolled and annealed prior to the FSBR experiment, which had a strain-free equiaxed grain structure with an average grain size of 24.9±1.9 μm. After the FSBR process, the material microstructure was examined near the rivet hole surface. The specimen was sectioned along the rivet axis and polished on a Struers polishing machine. The specimen's top surface was etched for 3 s with 0.5% HF followed by the standard electron backscatter diffraction (EBSD) analysis using CARL ZEISS scanning electron microscope. An illustration of the EBSD analysis area is shown in Fig. 1. Three different analysis step sizes were used for the analysis. A fine step size of 1 μm was used near the hole surface, and was gradually increased to 3 μm away from the hole surface. Average grain size was calculated by analyzing the micrograph using open source MATLAB program "linecut." The resultant microstructure after the FSBR process is examined in Fig. 2. It can be clearly seen that workpiece material underwent different microstructure evolution at the thermomechanically affected zones (TMAZs). Significant grain size refinement was observed near the friction stir penetrated hole surface after the process (Fig. 2(*a*)). The grain size was as low as 1–2 μm near the hole surface and gradually increased away from the hole surface. A zoom-in view of the microstructure near the hole surface is shown in Figs. 2(*b*) and 2(*c*). Beyond 350 μm, the average grain size was similar to the as-received material. According to the grain size, the processed microstructure was classified into zone I, II, III and unaffected zone (Fig. 2(*a*)). Zone I had a width of 25 μm from the hole surface, whereas zone II was 65 μm wide and zone III is 260 μm wide. Beyond zone III, there is no significant change of grain size after the FSBR process, so it is considered as an unaffected zone. Average grain size and microstructure in the unaffected zone are similar to the base material. In zone III, grains started to reduce in size. The average grain size reduced significantly to 14.3±1.0 μm. This indicates that amount of shear deformation started to increase from unaffected area to the zone III. As the hole surface is approached further, significantly smaller grains can be observed. In zone II, elongated grains with high aspect ratio can be seen as in Figs. 2(*a*) and 2(*b*). The grain size is reduced significantly and average grain width reduces to 6.76±0.58 μm. On the contrary, in the zone I, those elongated grains were dissolved and fine equiaxed grains had evolved (Fig. 2(*c*)). Average grain size was close to 1 μm and some grains were below 1 μm as well.

Table 1 Experimental conditions [20]

Materials	AA 6111-T4 (sheets) Zinc coated mild-steel (rivets)
Sheet thickness	0.9 mm
Rotational speed	6000 rpm
Feed rate	780 mm/min

2.2 Microstructure Evolution Mechanisms. The FSBR process involves sliding and sticking contact between rivet and

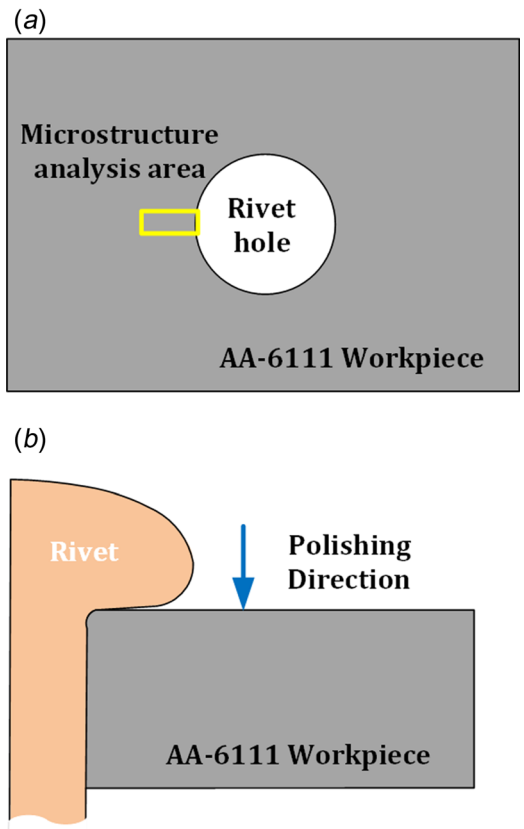

Fig. 1 An illustration of the FSBR microstructure analysis area: (*a*) top view and (*b*) cross section view

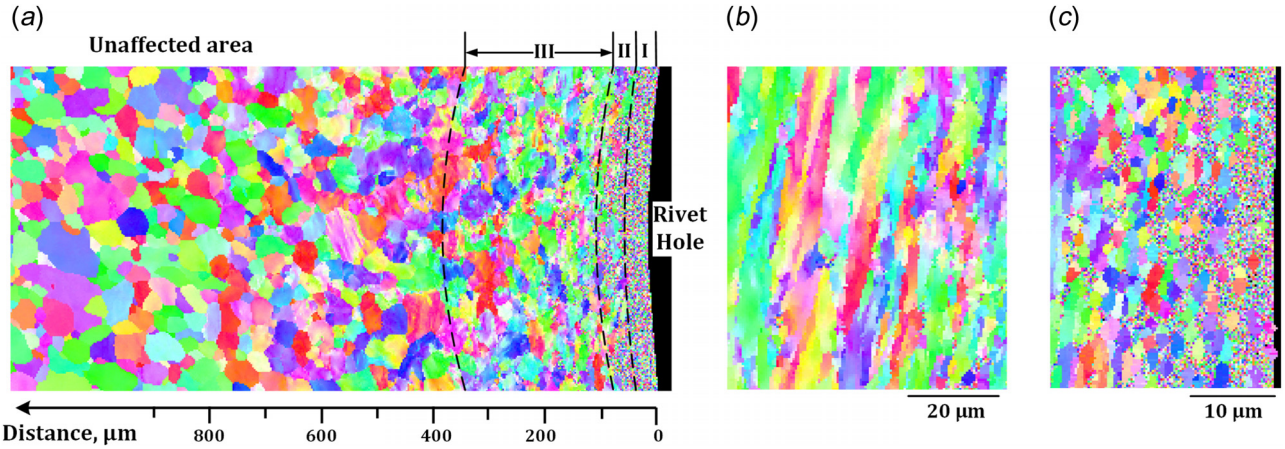

Fig. 2 Microstructure of the work material after FSBR: (*a*) overall grain structure indicating different evolution zones, (*b*) grain structure in zone II, and (*c*) grain structure in zone I near the rivet hole

workpiece material as in all friction stir processes [20]. When the high-speed rotating rivet penetrates into the workpiece, workpiece material adjacent to the hole partially sticks to the rivet surface and stirs during the process. As a result, the material undergoes severe plastic deformation, and the strain rate in this region is very high compared with the bulk material. The strain rate in the plastic deformation zone in friction stir processes is proportional to the rotational speed of the tool. It is in the order of $10–10^3$ s^{-1} depending on the rotating condition of the tool [42–44]. The maximum strain rate is near the surface of the tool and diminishes rapidly away from the tool [45,46]. This region also has a higher process temperature as it is very close to the frictional heat flux between base material and rivet. It is most likely that the temperature in this region reaches up to the recrystallization temperature range. Severe shear deformation also indicates that it should have stored enough strain energy to trigger the DRX [47–49]. At the same time, if the material undergoes severe plastic deformation, there is a higher rate of nucleation compared to the rate of growth [50]. Those newly nucleations have less space to grow. On the contrary, as away from the hole surface, less plastic deformation happens as the stirring effect reduces as distance increases. It also has low temperature as they are far from the frictional heat source. As a result, less nucleation happens in this region and those nucleate sites have more room for grain growth.

Three types of DRX have been characterized in hot deformation processes of aluminum alloys: (1) continuous dynamic recrystallization (cDRX) [51–53], (2) dDRX [54–57], and (3) geometric dynamic recrystallization (gDRX) [57–59]. During cDRX, new grains are formed due to the dislocation accumulation and misorientation increase between subgrains. In contrast, during dDRX, migration of high-angle boundaries (HABs) helps to form new grains with large angle boundaries by dynamic nucleation and grain growth [53,54]. gDRX has been observed at high temperatures and low-strain rates for some materials due to subgrain boundary formation and dynamic recovery [59]. Strain rate plays an important role to decide what kind of DRX mechanism happens during hot deformation of aluminum alloys. Both Humphreys and Hatherly [60] and Rokni et al. [58] observed that cDRX and gDRX are dominating mechanism at low strain rate, whereas dDRX occurs at high strain rate during hot deformation of aluminum alloys. Amount of HABs in EBSD analysis after a hot deformation process is also a good indication about dDRX mechanism [57]. Su et al. [54] observed that very small grains with high HABs are generated by dDRX from severely deformed Al alloy undergoing friction stir process.

During the FSBR process of this work, AA6111-T4 is severely deformed above recrystallization temperature, and high strains and temperature gradients exist in the processing zone. Material adjacent to the rivet tool experiences the highest strain, strain rate, and temperature, whereas material further away from the tool evolves under gradually decreasing strains, strain rates, and temperatures. As can be seen in Fig. 2, the work material adjacent to the rivet hole surface has a submicron and even nanoscale grain structure consisting of mainly HABs, which indicates that HABs create new grains directly from the severely deformed substructure during the FSBR process. Based on the EBSD data, thermomechanical loading conditions of the FSBR process, and prior research on DRX mechanisms of aluminum alloys during friction stir processes; it is concluded in this study that dDRX is the dominating mechanism of grain recrystallization within the region close to the rivet tool during the FSBR process.

3 Friction Stir Blind Riveting Process Model

An FSBR process model was developed in this work based on a mesh-free SPH method, which was used to determine the thermomechanical loading conditions needed by the subsequent CA microstructure evolution model. Previous research has demonstrated that SPH mesh and FEM mesh can be used to model the work material and tool, respectively, to simulate severe deformation processes such as metal cutting [61] and friction stir welding [42,62,63]. Since the SPH model does not need a predefined failure surface, remeshing or eroding of elements, material flow simulation by tracking the movement of SPH elements is more efficient. In this work, to reduce the computation time, the steel rivet was considered as a rigid body with FEM elements, while AA6111-T4 workpiece was modeled using SPH elements with symmetric boundary. The friction coefficient was considered as 0.7 between the blind rivet and workpiece. Since the workpiece domain was limited to save the computational cost, releasing heat flux was applied at the boundaries to dissipate heat. Table 2 lists physical and mechanical properties of the workpiece and rivets used in the process model. The process simulation was performed using computational software LS-DYNA [66]. Figure 3 shows the simulated steady-state temperature distribution. The temperature

Table 2 Material properties used in the SPH model [64,65]

Property	AA6111-T4 (workpiece)	Steel (rivet)
Density (kg/m^3)	2710	7800
Young's modulus (GPa)	70	200
Poisson's ratio	0.33	0.30
Yield strength (MPa)	165	386
Thermal conductivity (W/m° C)	167	47.7
Heat capacity (J/kg° C)	996	432.6

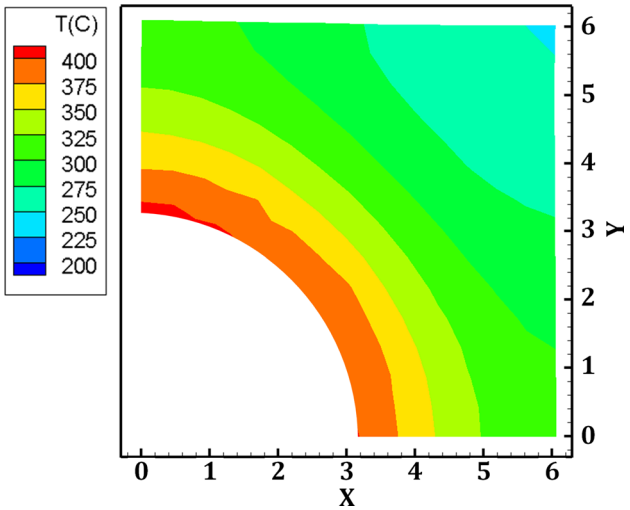

Fig. 3 Simulated temperature distribution around the friction stir penetrated hole surface

was around 400 °C at the penetrated hole surface and went down away from the hole surface.

4 Cellular Automaton Model

In this study, a CA model was developed in MATLAB to simulate the evolution of microstructure during the FSBR process. In this CA model, the simulation domain was discretized into an array of equally spaced lattice cells. Multiple state variables representing crystal orientation, grain boundary, dislocation density, recrystallization, etc. were allocated to each lattice cell. During the CA simulations, the state variables were updated, and lattice cells evolved according to the states of its neighboring cells following a given set of transformation rules.

4.1 Model Assumptions. The following describes several basic assumptions implemented in this CA model:

(1) A homogenous material structure without any crystalline defect was assumed as the initial condition. Grain rotation was not considered in this numerical model. The work material AA6111-T4 alloy was solutionized and naturally aged prior to the FSBR experiment. An initial dislocation density of $10^{10}\,\mathrm{m}^{-2}$ (a typical level for a well-annealed aluminum alloy [67,68]) was therefore applied across the work material domain.
(2) Dislocations and grain boundary energy were considered as the driving forces of recrystallization. The effect of the elastic strain energy and surface energy was not considered.
(3) dDRX was considered as the major recrystallization mechanism in this study. Grain nucleation happens only at the grain boundary, which comprises both primary and recrystallized grain boundaries, and occurs as the dislocation density attains the critical level. The critical value of dislocation density depends on two important process loading conditions, i.e., strain rate and temperature [25,69]. It was assumed that newly recrystallized grains have a low level of dislocation density.

4.2 Modeling of Dislocation Density Evolution. The dislocation density of work material evolves as it undergoes work hardening and dynamic recovery (softening), sometimes simultaneously, during a deformation process. The evolution of material dislocation density greatly influenced the nucleation, dDRX, and grain growth. Phenomenological KM model proposed by Kocks and Mecking [70,71] was implemented to model the change of dislocation density during stage III hardening. This model considers that dislocation density (ρ) is the single structural parameter that control the kinetics of plastic flow of materials, which is shown below [72]:

$$\frac{\partial \rho}{\partial \varepsilon} = k_1\sqrt{\rho} + \frac{1}{bd} - k_2\rho \tag{1}$$

where ε is the strain; k_1 and k_2 are material constants; b represents Burger's vector; and d is the mean grain size. The first term on the right side of Eq. (1) signifies the increase in dislocation density due to work hardening, while the second and third terms indicate the effect of dynamic recovery.

The occurrence of nucleation during DRX was determined as the dislocations were accumulated due to severe plastic deformation. As the dislocation density in the deformed work material reaches the critical dislocation density, nuclei will start to generate on grain boundaries for DRX during the thermomechanical process. Following Roberts and Ahlblom [73], the critical value of dislocation density for DRX nucleation was determined using the below equation:

$$\rho_{\mathrm{crit}} = \left(\frac{20\gamma_m\dot{\varepsilon}}{3blM\tau^2}\right)^{1/3} \tag{2}$$

where γ_m is the grain boundary energy associated with conversion to high-angle boundary; M is mobility of grain boundary; $\dot{\varepsilon}$ is strain rate; and τ is the dislocation line energy. The grain boundary energy γ_m is given by

$$\gamma_m = \frac{Gb\theta_m}{4\pi(1-\nu)} \tag{3}$$

where G is the material shear modulus; θ_m is the misorientation associated with a high-angle boundary (here, it was assumed as $\pi/12$ rad); and ν is Poisson's ratio. The dislocation mean free path (l) is expressed as [74]

$$l = \frac{c_1 Gb}{\sigma} \tag{4}$$

where c_1 is material constant (it was assumed 10 for most metals [75]) and σ represents the flow stress of the material. The mobility of grain boundary (M) is calculated by [76,77]

$$M = \frac{\delta D_{0b} b}{KT}\exp\left(-\frac{Q_b}{RT}\right) \tag{5}$$

where δ is the grain boundary thickness of the material; K is the Boltzmann constant; D_{0b} is grain boundary self-diffusion coefficient at 0 Kelvin; Q_b is grain boundary diffusion activation energy; R is the ideal gas constant; and T is temperature in Kelvin. The dislocation line energy τ is calculated based on [60]

$$\tau = c_2 Gb^2 \tag{6}$$

where c_2 is a material constant.

4.3 Modeling of Nucleation Rate. In this study, nucleation rate $\dot{n}(\dot{\varepsilon}, T)$ was calculated using Eq. (7) based on the model proposed by Ding and Guo [25], which incorporates the influences of processing temperature [69] and strain rate [78]

$$\dot{n}(\dot{\varepsilon}, T) = C\dot{\varepsilon}^m \exp\left(-\frac{Q_{\mathrm{act}}}{RT}\right) \tag{7}$$

where C is a material constant; exponent m is a constant (it was assumed as 1 [25]); Q_{act} is the activation energy. The DRX percentage η was then calculated by

Table 3 CA model parameters [25,60,75,80,81]

Variable	k_1	k_2	b (nm)	G (GPa)	θ_m (rad)	N	c_1	δD_{0b} (m^3 s^{-1})
Value	2.26×10^9	76.36	0.286	25.9	$\pi/12$	0.33	10	5.0×10^{-14}
Variable	K (m^2 kg s^{-2} K^{-1})	Q_b (kJ mol^{-1})	R (J mol^{-1} K^{-1})	c_2	C	m	Q_{act} (kJ mol^{-1})	c_3
Value	1.38×10^{-23}	82	8.314	0.5	8.0×10^{24}	1	142	10

$$\eta = \dot{n}\frac{\varepsilon}{\dot{\varepsilon}}\frac{4}{3}\pi r_d^3 \tag{8}$$

where r_d represents the average radius of all the recrystallized grains. It is determined using

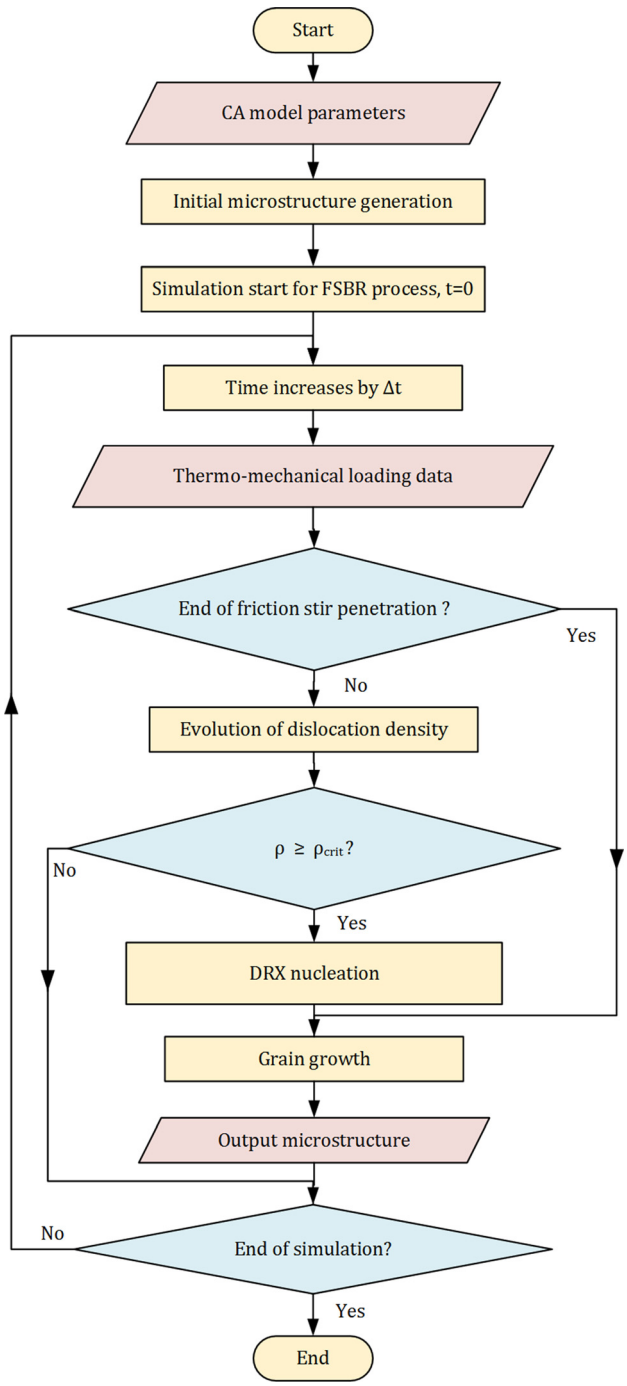

Fig. 4 Flowchart for CA model

$$\frac{\sigma_s}{G}\left(\frac{2r_d}{b}\right)^n = c_3 \tag{9}$$

where σ_s represents the steady-state flow stress, n is a constant (its value is 2/3), and c_3 is a material constant.

4.4 Modeling of Recrystallized Grain Growth. Difference in dislocation density between the matrix and recrystallized grains provides the driving force for grain growth of the newly created nucleation sites. The grain boundary tends to move from recrystallized grains toward grains with high dislocation density. For recrystallization grains, their growth rate follows:

$$V_i = Mf_i \tag{10}$$

where f_i represents driving force per unit area for the growth of recrystallized grains and it is represented by the following formula:

$$f_i = \tau(\rho_m - \rho_i) - 2\frac{\gamma_i}{d_i} \tag{11}$$

where ρ_m and ρ_i represent the dislocation density of matrix grains and recrystallized grains, respectively; d_i and γ_i stand for the diameter of recrystallized grains and the grain boundary energy, respectively. γ_i is calculated by Read and Shockley [79]

$$\gamma_i = \begin{cases} \gamma_m \dfrac{\theta_i}{\theta_m}\left[1 - \ln\left(\dfrac{\theta_i}{\theta_m}\right)\right] & \text{for} \quad \theta_i \le \theta_m \\ \gamma_m & \text{for} \quad \theta_i > \theta_m \end{cases} \tag{12}$$

where θ_i is the orientation difference between the recrystallized grains i and its neighboring grains.

The material parameters used for the CA simulation of AA 6111-T4 are listed in Table 3.

4.5 CA Simulations. A grain growth algorithm was developed to generate the initial microstructure before FSBR simulation. The simulation domain was set as 400 μm × 200 μm with a square cell size of 1.0 μm × 1.0 μm. The step time required for growth of a cell was considered as below:

$$\Delta t = \frac{L_{CA}}{M\Delta F_{max}} \tag{13}$$

where L_{CA} is unit cell side length and ΔF_{max} is the maximum grain boundary migration driving force. The strain increment within this time-step can be expressed as

$$\Delta\varepsilon = \dot{\varepsilon}\Delta t = \dot{\varepsilon}\frac{L_{CA}}{M\Delta F_{max}} \tag{14}$$

The simulated temperature distribution and history were applied as the thermal loading condition for the CA simulation. The CA model assumed a strain rate of 10^3 s^{-1} at the tool–workpiece interface [42,44], and it reduces exponentially as it reaches to the other side of the simulation domain [46]. The CA simulation was performed for a single pass of friction stir penetration. The detailed steps for the simulation are as follows:

(1) CA model parameters are defined as listed in Table 3, and the thermomechanical loading conditions are applied. Then, the initial grain structure is generated.
(2) Dislocation density is updated using the models given in Sec. 4.1 for each time step. The mean dislocation density at different times was determined by

$$\bar{\rho} = \frac{1}{NN}\sum_{i}^{NN}\rho_i \tag{15}$$

where ρ_i is the dislocation density at the cell site and NN represents the total number of cells in the simulation region.
(3) Nucleation of recrystallized grain was randomly distributed along the grain boundary during the simulation of CA. For a particular timestep, the nucleation probability for a certain cell was given by

$$p_{\text{nuc}} = \dot{n} \times \Delta t \times S_{\text{CA}} \tag{16}$$

where S_{CA} was the area of the unit cell, for square cells, $S_{\text{CA}} = L_{\text{CA}}^2$. A random number rand was generated for each timestep. If rand $< p_{\text{nuc}}$, the cell became a DRX nucleus and the dislocation density variable was set to a very small number. If rand $> p_{\text{nuc}}$, the cell did not undergo DRX nucleation.

(4) The newly recrystallized grains would continue to grow and the grain boundary would migrate continuously. The migration distance of recrystallized grain boundaries for each time step was determined by

$$L_G = V_i \Delta t \tag{17}$$

and the radius of this recrystallized grains r is given as [33]

$$r = \sqrt{N_{\text{DRX}} \cdot S_{\text{CA}}/\pi} \tag{18}$$

where N_{DRX} is the total number of the CA cells held by this recrystallized grain. As the grain growth rate V_i is reduced to zero, the grain growth stops. The recrystallization progress is captured by the volume fraction of recrystallized grains, X_{DRX}

$$X_{\text{DRX}} = \frac{N_{\text{DRX}}}{N_X \cdot N_Y} \tag{19}$$

where N_{DRX} is the total cell number in recrystallized grains, and N_X and N_Y are the total cell numbers along X-axis and Y-axis, respectively, in the two-dimensional simulation domain.

Once a recrystallized grain collides with other recrystallized grains, they stop growing in the same direction at the same time. The detailed flow chart is shown in Fig. 4.

5 Results and Discussion

Figure 5 shows the comparison of the simulated initial microstructure to EBSD analysis prior to the FSBR process. The mean diameter of primary grains before the simulation was 26.5 ± 1.8 μm. This is close to the experimental measurement of 24.9 ± 1.9 μm. Exact match is not necessary, as the initial microstructure generation algorithm was based on the random allocation of nucleation points.

The driving force for grain structure evolution during the FSBR process is associated with the change of dislocation density distribution as shown in Figs. 6 and 7. The right boundary of the simulation domain was physically equivalent to the hole surface. This boundary had a higher temperature and strain rate compared to the left boundary as this boundary was the source of the frictional heat generation and material stirring. As the AA 6111 workpiece is solutionized and naturally aged, a uniform initial dislocation density of 10^{10} m^{-2} (typical level for a well-annealed aluminum alloy [67,68]) was applied across the whole domain as initial dislocation density. As the simulation started, the dislocation density on the right side boundary increased faster as shown in Fig. 6(*a*) compared to the left boundary as the dislocation density is proportional to strain and strain rate and right boundary possessed higher strain and strain rate. The dislocation density quickly rose to 2×10^{14} m^{-2}. When the dislocation density of a particular grain went beyond the critical dislocation density, sporadic dark areas, as shown in Fig. 6(*b*), were generated near the right side boundary. Each dark area corresponds to the domain of DRX nuclei. Dislocation density of the newly grown recrystallized grain was reset to the initial dislocation density, which lowered the mean dislocation density at the right boundary at the onset of DRX as shown in Fig. 7. As the simulation progress, more recrystallized grains away from right boundary formed until the completion of DRX and new dark areas were observed as shown in Fig. 6(*c*). Researchers have experimentally observed using X-ray and Neutron diffraction method that mean dislocation density is $\sim 1.7 \times 10^{14}$ m^{-2} and $3 \times 10^{15} \sim 11 \times 10^{15}$ m^{-2} in dynamic recrystallized zone and other TMAZ zones, respectively, of an unsolutionized AA 6061 undergoing friction stir welding process [82,83]. The simulated mean dislocation density in the current simulation of the FSBR process was $1.5 \times 10^{13} \sim 6 \times 10^{14}$ m^{-2} in the dynamic recrystallized area and $\sim 1.5 \times 10^{15}$ m^{-2} in the rest of the TMAZ zone. The simulated mean dislocation density is little smaller compared to the reported experimentally measured values for friction stir processes because the initial workpiece was solutionized and naturally aged and therefore had lower initial dislocation density compared to reported values.

After the frictional penetration was finished during the FSBR process, there was no more frictional heat generation, so the work material started cooling. As the bulk material was still at low

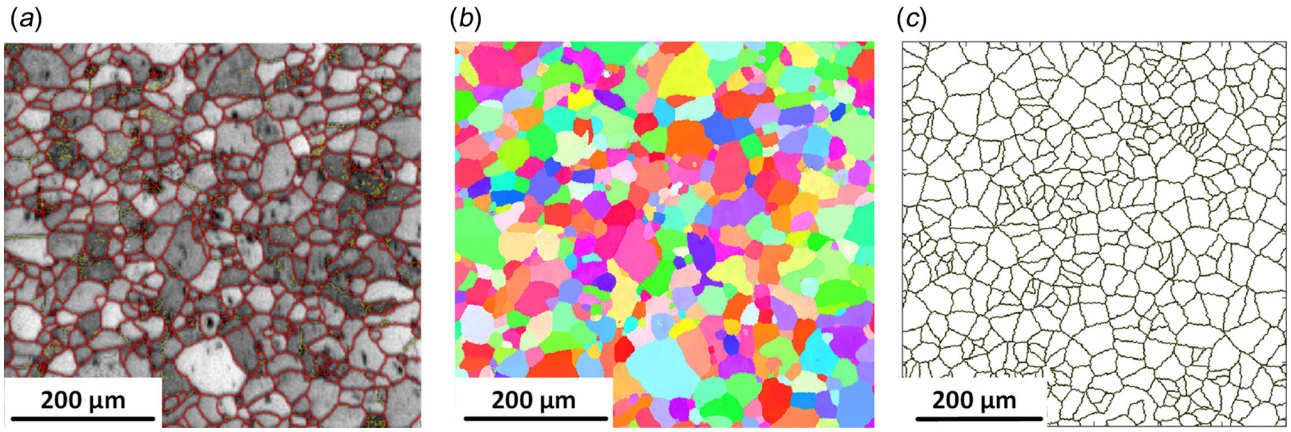

Fig. 5 Comparison of the initial microstructure of AA6111-T4 prior to FSBR process: (*a*) EBSD micrograph, (*b*) EBSD crystal orientation maps [20], and (*c*) simulated initial microstructure

temperature, the cooling rate was very fast. As a result, the DRX nucleation stopped very quickly and only grain growth happened thereafter. The final dislocation density distribution after the completion of the FSBR process is shown in Fig. 6(*d*). During the cooling cycle, the mean dislocation density kept decreasing over the whole simulation domain (Fig. 7) as the newly recrystallized grains with low dislocation density grew and consume other grains with higher dislocation density. The final mean dislocation density in the recrystallized zone varies between 1.5×10^{13} m^{-2} and 6×10^{14} m^{-2}, which is very close to experimentally reported values of 1.7×10^{14} m^{-2} [82].

Quantitative assessment of CA simulation results was performed by comparing with the corresponding temperature histories from process simulations. Figure 8(*a*) shows the history of the process temperature on the rivet hole surface during severe plastic deformation as well as cooling cycle. During the deformation cycle, temperature reached up to 400 °C on the rivet hole surface and then cooled down quickly after the frictional penetration is completed. The CA simulated recrystallization process was dependent on the process temperature history. The dDRX nucleus started to form at the moment when the process temperature increased to about $0.4T_m$ (critical level of temperature for the onset of DRX [47,48]). In addition, the thermally driven grain growth during the cooling cycle was usually ceased when the temperature dropped to the level about $0.5T_m$ [47,48]. The matrix microstructure was not completely replaced with the recrystallized grains, and the X_{DRX} stopped at 0.66 (Fig. 8(*b*)). DRX only happened adjacent to the hole surface. As the temperature and strain rate are low away from the hole, no DRX took place.

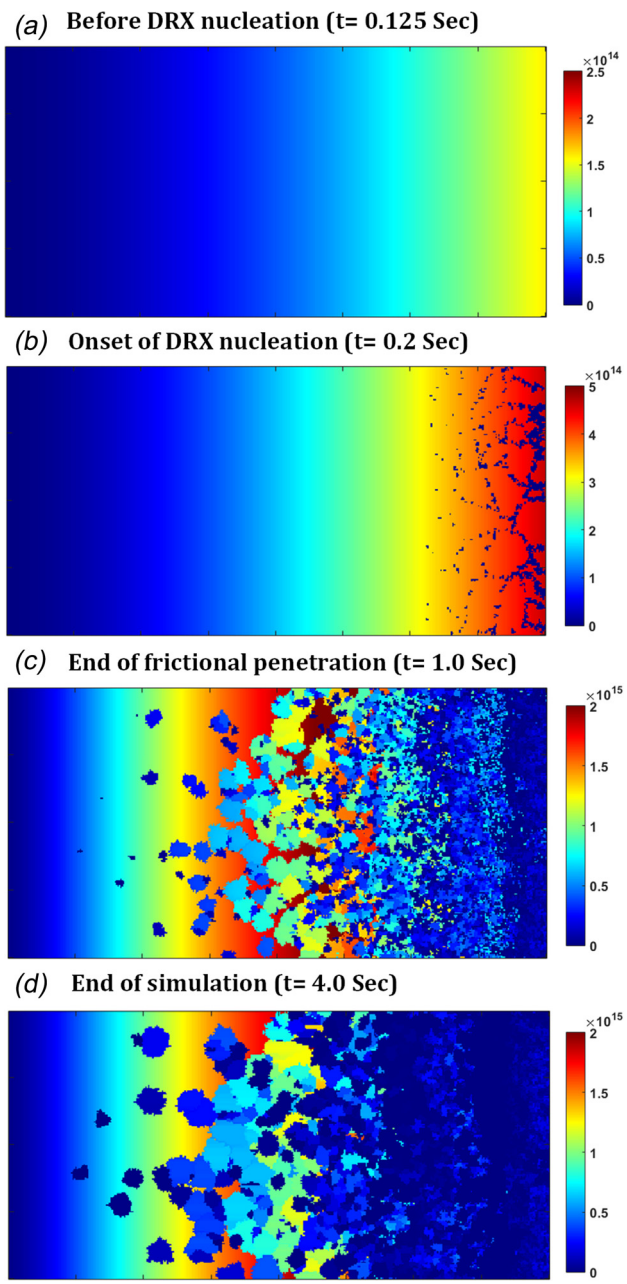

Fig. 6 Simulated contour plot of dislocation density at different stage of the process: (*a*) before DRX nucleation, (*b*) onset of DRX nucleation, (*c*) end of frictional penetration, and (*d*) end of simulation

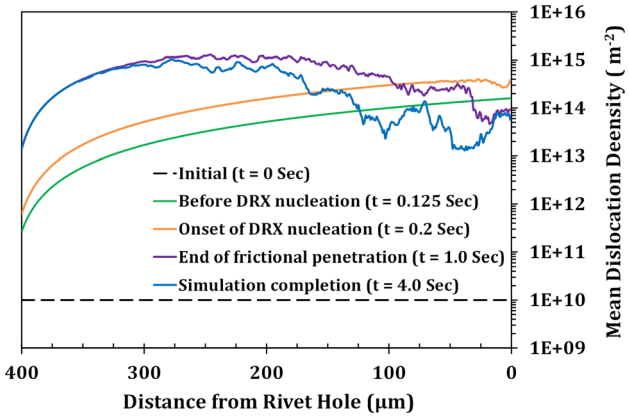

Fig. 7 Spatial evolution of mean dislocation density

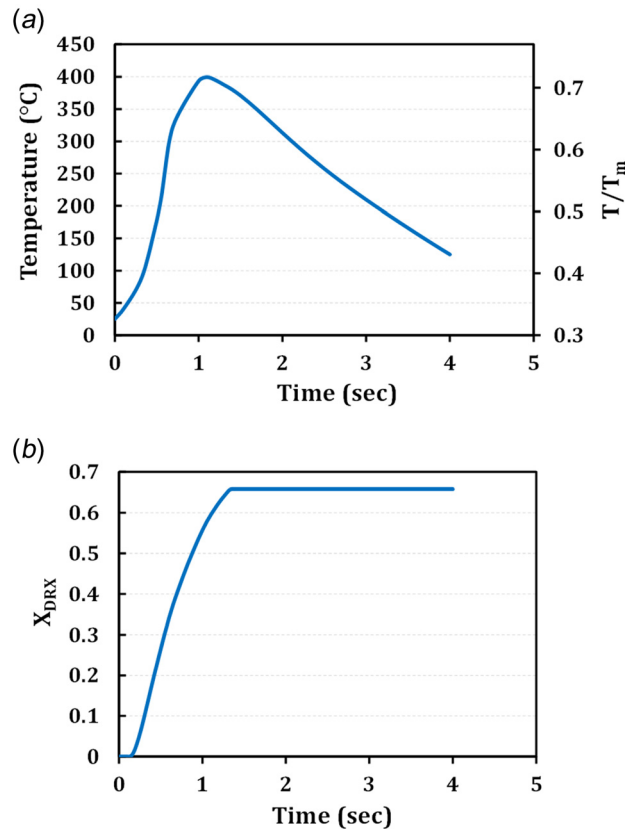

Fig. 8 The recrystallization progress histories of (*a*) the simulated temperature history of hole surface and (*b*) volume fraction of the recrystallized domain

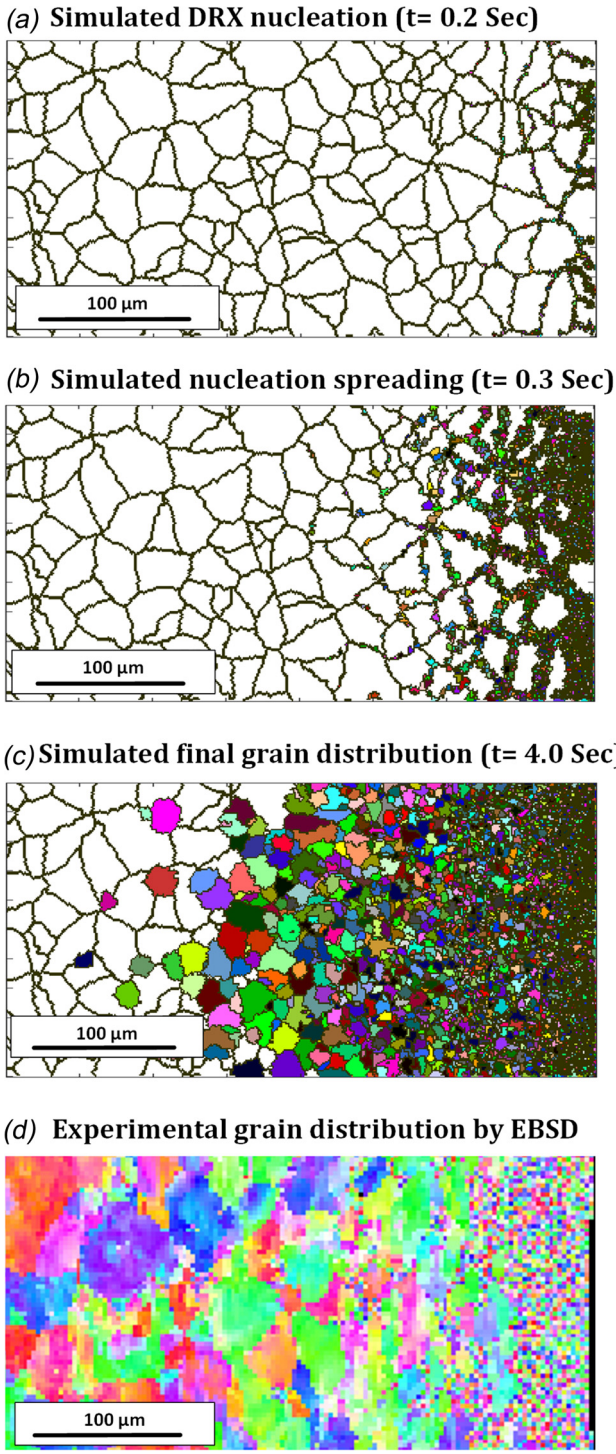

Fig. 9 Evolution of microstructure during CA simulation: (*a*) DRX nucleation near the right side boundary, (*b*) DRX nucleation spread toward left boundary, (*c*) final simulated grain structure, and (*d*) experimental grain structure (experimental images adapted from Ref. [20]

The simulated microstructure evolution of the AA6111-T4 during FSBR process is shown in Figs. 9(*a*)–9(*c*) under the thermomechanical condition across the simulation domain. The DRX nucleation first starts near the right side boundary (Fig. 9(*a*)) and then spread toward left boundary subsequently as shown in Fig. 9(*b*). Figure 9(*d*) shows the experimental EBSD measurement of microstructure distribution after the completion of FSBR process. It agrees well with final simulated microstructure as shown in Fig. 9(*c*). The simulated grain size is calculated in different zones based on the zone width calculated from experimental result. The simulation result shows that the right boundary has smaller grain size 2.35±0.05 μm, which is very close to experimentally measured value of 1.94±0.09. This error might be attributed from the assigned temperature boundary conditions in the simulation as it is very difficult to capture accurate temperature distribution in such a small resolution.

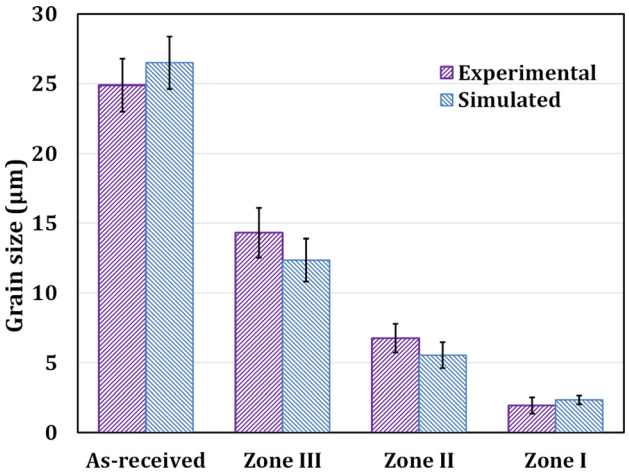

Fig. 10 Simulated grain size comparison

Figure 10 compares the simulated grain distribution across different zones with experimentally measured values. Our current analysis domain is based on the zones I, II, and III as mentioned in Sec. 2. The simulated average grain size agrees well with the experimentally calculated grain sizes.

As a final note, the evolution of submicron grains is not captured in this model. The resolution of the simulation domain is currently limited to 1 μm. As a result, this model is unable to capture the submicron grains near the hole edge. The future goal is to implement gradient resolution across the analysis domain by modifying the model parameters as a function of resolution.

6 Conclusions

The evolution of microstructure by DRX in the friction stir blind riveting process is first time successfully modeled using CA method. A MATLAB code has been developed to implement the CA method to capture the microstructure evolution during the process. The DRX of grains is modeled based on the evolution of dislocation density during the process loading condition in terms of temperature, strain rate, and strain distribution across the domain.

The simulation results demonstrated that the high temperature and strain rate distribution at the friction stir riveted hole triggered DRX. The final grain size distribution is predicted and validated with experimental measurement. The simulated initial grain size distribution agreed well with the experimental EBSD measurement, so the developed CA model is validated. This model is a computation-efficient numerical approach to predict the evolution of microstructure governed by dDRX under the large plastic deformation gradient.

Funding Data

- National Science Foundation (Grant Nos. CMMI-1537512 and CMMI 1651024).

References

[1] Wang, P.-C., and Stevenson, R., 2006, "Friction Stir Rivet Method of Joining," Gm Global Technology Operations, Inc., Detroit, MI, U.S. Patent No. US7,862,271.

[2] Gao, D., Ersoy, U., Stevenson, R., and Wang, P., 2009, "A New One-Sided Joining Process for Aluminum Alloys: Friction Stir Blind Riveting," ASME J. Manuf. Sci. Eng., **131**(6), p. 061002.
[3] Min, J., Li, J., Li, Y., Carlson, B. E., Lin, J., and Wang, W.-M., 2015, "Friction Stir Blind Riveting for Aluminum Alloy Sheets," J. Mater. Process. Technol., **215**, pp. 20–29.
[4] Min, J., Li, Y., Carlson, B. E., Hu, S. J., Li, J., and Lin, J., 2015, "A New Single-Sided Blind Riveting Method for Joining Dissimilar Materials," CIRP Ann.-Manuf. Technol., **64**(1), pp. 13–16.
[5] Lathabai, S., Tyagi, V., Ritchie, D., Kearney, T., Finnin, B., Christian, S., Sansome, A., and White, G., 2011, "Friction Stir Blind Riveting: A Novel Joining Process for Automotive Light Alloys," SAE Int. J. Mater. Manuf., **4**(1), pp. 589–601.
[6] Min, J., Li, J., Carlson, B. E., Li, Y., Quinn, J. F., Lin, J., and Wang, W., 2015, "Friction Stir Blind Riveting for Joining Dissimilar Cast Mg AM60 and Al Alloy Sheets," ASME J. Manuf. Sci. Eng., **137**(5), p. 51022.
[7] Wang, W.-M., Ali Khan, H., Li, J., Miller, S. F., and Trimble, A. Z., 2017, "Classification of Failure Modes in Friction Stir Blind Riveted Lap-Shear Joints With Dissimilar Materials," ASME J. Manuf. Sci. Eng., **139**(2), p. 021005.
[8] Min, J., Li, Y., Li, J., Carlson, B. E., and Lin, J., 2015, "Friction Stir Blind Riveting of Carbon Fiber-Reinforced Polymer Composite and Aluminum Alloy Sheets," Int. J. Adv. Manuf. Technol., **76**(5–8), pp. 1403–1410.
[9] Jata, K. V., and S, S. L., 2000, "Continuous Dynamic Recrystallization During Friction Stir Welding of High Strength Aluminum Alloys," Scr. Mater., **43**(8), pp. 743–749.
[10] McNelley, T. R., Swaminathan, S., and Su, J. Q., 2008, "Recrystallization Mechanisms During Friction Stir Welding/Processing of Aluminum Alloys," Scr. Mater., **58**(5), pp. 349–354.
[11] Liu, G., Murr, L. E., Niou, C.-S., McClure, J. C., and Vega, F. R., 1997, "Microstructural Aspects of the Friction-Stir Welding of 6061-T6 Aluminum," Scr. Mater., **37**(3), pp. 355–361.
[12] Murr, L., Liu, G., and McClure, J., 1997, "Dynamic Recrystallization in Friction-Stir Welding of Aluminium Alloy 1100," J. Mater. Sci. Lett., **16**(22), pp. 1801–1803.
[13] Cao, X., and Jahazi, M., 2011, "Effect of Tool Rotational Speed and Probe Length on Lap Joint Quality of a Friction Stir Welded Magnesium Alloy," Mater. Des., **32**(1), pp. 1–11.
[14] Mironov, S., Onuma, T., Sato, Y. S., and Kokawa, H., 2015, "Microstructure Evolution During Friction-Stir Welding of AZ31 Magnesium Alloy," Acta Mater., **100**(18), pp. 301–312.
[15] Lienert, T., and Stellwag, W., Jr., 2003, "Friction Stir Welding Studies on Mild Steel," Weld. J., **82**(1), pp. 1–9.
[16] Saeid, T., Abdollah-Zadeh, A., Shibayanagi, T., Ikeuchi, K., and Assadi, H., 2010, "On the Formation of Grain Structure During Friction Stir Welding of Duplex Stainless Steel," Mater. Sci. Eng. A, **527**(24–25), pp. 6484–6488.
[17] Mohammadi, J., Behnamian, Y., Mostafaei, A., Izadi, H., Saeid, T., Kokabi, A. H., and Gerlich, A. P., 2015, "Friction Stir Welding Joint of Dissimilar Materials Between AZ31B Magnesium and 6061 Aluminum Alloys: Microstructure Studies and Mechanical Characterizations," Mater. Charact., **101**, pp. 189–207.
[18] Chang, W. S., Rajesh, S. R., Chun, C. K., and Kim, H. J., 2011, "Microstructure and Mechanical Properties of Hybrid Laser-Friction Stir Welding Between AA6061-T6 Al Alloy and AZ31 Mg Alloy," J. Mater. Sci. Technol., **27**(3), pp. 199–204.
[19] Chen, Y. C., and Nakata, K., 2009, "Effect of Tool Geometry on Microstructure and Mechanical Properties of Friction Stir Lap Welded Magnesium Alloy and Steel," Mater. Des., **30**(9), pp. 3913–3919.
[20] Min, J., Li, J., Li, Y., Carlson, B. E., and Lin, J., 2016, "Affected Zones in an Aluminum Alloy Frictionally Penetrated by a Blind Rivet," ASME J. Manuf. Sci. Eng., **138**(5), p. 054501.
[21] Rotella, G., Dillon, O. W., Umbrello, D., Settineri, L., and Jawahir, I. S., 2013, "Finite Element Modeling of Microstructural Changes in Turning of AA7075-T651 Alloy," J. Manuf. Process., **15**(1), pp. 87–95.
[22] Tabei, A., Shih, D. S., Garmestani, H., and Liang, S. Y., 2016, "Dynamic Recrystallization of Al Alloy 7075 in Turning," ASME J. Manuf. Sci. Eng., **138**(7), p. 071010.
[23] Zheng, C., Xiao, N., Li, D., and Li, Y., 2008, "Microstructure Prediction of the Austenite Recrystallization During Multi-Pass Steel Strip Hot Rolling: A Cellular Automaton Modeling," Comput. Mater. Sci., **44**(2), pp. 507–514.
[24] Kugler, G., and Turk, R., 2004, "Modeling the Dynamic Recrystallization Under Multi-Stage Hot Deformation," Acta Mater., **52**(15), pp. 4659–4668.
[25] Ding, R., and Guo, Z. X., 2001, "Coupled Quantitative Simulation of Microstructural Evolution and Plastic Flow During Dynamic Recrystallization," Acta Mater., **49**(16), pp. 3163–3175.
[26] Yin, H., and Felicelli, S. D., 2009, "A Cellular Automaton Model for Dendrite Growth in Magnesium Alloy AZ91," Modell. Simul. Mater. Sci. Eng., **17**(7), p. 75011.
[27] Yazdipour, N., Davies, C. H. J., and Hodgson, P. D., 2008, "Microstructural Modeling of Dynamic Recrystallization Using Irregular Cellular Automata," Comput. Mater. Sci., **44**(2), pp. 566–576.
[28] Jin, Z., and Cui, Z., 2010, "Investigation on Strain Dependence of Dynamic Recrystallization Behavior Using an Inverse Analysis Method," Mater. Sci. Eng. A, **527**(13–14), pp. 3111–3119.
[29] Jin, Z., and Cui, Z., 2012, "Investigation on Dynamic Recrystallization Using a Modified Cellular Automaton," Comput. Mater. Sci., **63**, pp. 249–255.
[30] Chen, F., Cui, Z., Liu, J., Zhang, X., and Chen, W., 2009, "Modeling and Simulation on Dynamic Recrystallization of 30Cr2Ni4MoV Rotor Steel Using the Cellular Automaton Method," Modell. Simul. Mater. Sci. Eng., **17**(7), p. 075015.
[31] Chen, F., Cui, Z., Liu, J., Chen, W., and Chen, S., 2010, "Mesoscale Simulation of the High-Temperature Austenitizing and Dynamic Recrystallization by Coupling a Cellular Automaton With a Topology Deformation Technique," Mater. Sci. Eng. A, **527**(21–22), pp. 5539–5549.
[32] Chen, F., and Cui, Z., 2012, "Mesoscale Simulation of Microstructure Evolution During Multi-Stage Hot Forging Processes," Model. Simul. Mater. Sci. Eng., **20**(4), p. 45008.
[33] Chen, F., Qi, K., Cui, Z., and Lai, X., 2014, "Modeling the Dynamic Recrystallization in Austenitic Stainless Steel Using Cellular Automaton Method," Comput. Mater. Sci., **83**, pp. 331–340.
[34] Hallberg, H., Wallin, M., and Ristinmaa, M., 2010, "Simulation of Discontinuous Dynamic Recrystallization in Pure Cu Using a Probabilistic Cellular Automaton," Comput. Mater. Sci., **49**(1), pp. 25–34.
[35] Goetz, R., 2005, "Particle Stimulated Nucleation During Dynamic Recrystallization Using a Cellular Automata Model," Scr. Mater., **52**(9), pp. 851–856.
[36] Qian, M., and Guo, Z. X., 2004, "Cellular Automata Simulation of Microstructural Evolution During Dynamic Recrystallization of an HY-100 Steel," Mater. Sci. Eng. A, **365**(1–2), pp. 180–185.
[37] Xiao, N., Zheng, C., Li, D., and Li, Y., 2008, "A Simulation of Dynamic Recrystallization by Coupling a Cellular Automaton Method With a Topology Deformation Technique," Comput. Mater. Sci., **41**(3), pp. 366–374.
[38] Ding, H., Liu, L., Kamado, S., Ding, W., and Kojima, Y., 2009, "Investigation of the Hot Compression Behavior of the Mg–9Al–1Zn Alloy Using EBSP Analysis and a Cellular Automata Simulation," Model. Simul. Mater. Sci. Eng., **17**(2), p. 25009.
[39] Liu, X., Li, L., He, F., Zhou, J., Zhu, B., and Zhang, L., 2013, "Simulation on Dynamic Recrystallization Behavior of AZ31 Magnesium Alloy Using Cellular Automaton Method Coupling Laasraoui–Jonas Model," Trans. Nonferrous Met. Soc. China, **23**(9), pp. 2692–2699.
[40] Wu, C., Yang, H., and Li, H., 2013, "Modeling of Static Coarsening of Two-Phase Titanium Alloy in the $\alpha + \beta$ Two-Phase Region at Different Temperature by a Cellular Automata Method," Chin. Sci. Bull., **58**(24), pp. 3023–3032.
[41] Zhang, Y., Jiang, S., Liang, Y., and Hu, L., 2013, "Simulation of Dynamic Recrystallization of NiTi Shape Memory Alloy During Hot Compression Deformation Based on Cellular Automaton," Comput. Mater. Sci., **71**, pp. 124–134.
[42] Pan, W., Li, D., Tartakovsky, A. M., Ahzi, S., Khraisheh, M., and Khaleel, M., 2013, "A New Smoothed Particle Hydrodynamics Non-Newtonian Model for Friction Stir Welding: Process Modeling and Simulation of Microstructure Evolution in a Magnesium Alloy," Int. J. Plast., **48**, pp. 189–204.
[43] Arora, A., Zhang, Z., De, A., and DebRoy, T., 2009, "Strains and Strain Rates During Friction Stir Welding," Scr. Mater., **61**(9), pp. 863–866.
[44] Schmidt, H. B., and Hattel, J. H., 2008, "Thermal Modelling of Friction Stir Welding," Scr. Mater., **58**(5), pp. 332–337.
[45] Nandan, R., DebRoy, T., and Bhadeshia, H. K. D. H., 2008, "Recent Advances in Friction-Stir Welding—Process, Weldment Structure and Properties," Prog. Mater. Sci., **53**(6), pp. 980–1023.
[46] Nandan, R., Roy, G. G., Lienert, T. J., and Debroy, T., 2007, "Three-Dimensional Heat and Material Flow During Friction Stir Welding of Mild Steel," Acta Mater., **55**(3), pp. 883–895.
[47] Shen, N., Samanta, A., Ding, H., and Cai, W. W., 2016, "Simulating Microstructure Evolution of Battery Tabs During Ultrasonic Welding," SME J. Manuf. Process., **23**, pp. 306–314.
[48] Behnagh, R. A., Shen, N., Ansari, M. A., Narvan, M., Besharati Givi, M. K., and Ding, H., 2015, "Experimental Analysis and Microstructure Modeling of Friction Stir Extrusion of Magnesium Chips," ASME J. Manuf. Sci. Eng., **138**(4), p. 041008.
[49] Shen, N., Samanta, A., and Ding, H., 2017, "Microstructure Simulations for Orthogonal Cutting Via a Cellular Automaton Model," Procedia CIRP, **58**, pp. 543–548.
[50] Sellars, C. M., and Whiteman, J. A., 1979, "Recrystallization and Grain Growth in Hot Rolling," Met. Sci., **13**(3–4), pp. 187–194.
[51] Gourdet, S., and Montheillet, F., 2003, "A Model of Continuous Dynamic Recrystallization," Acta Mater., **51**(9), pp. 2685–2699.
[52] Bacca, M., Hayhurst, D. R., and McMeeking, R. M., 2015, "Continuous Dynamic Recrystallization During Severe Plastic Deformation," Mech. Mater., **90**, pp. 148–156.
[53] Sakai, T., Belyakov, A., Kaibyshev, R., Miura, H., and Jonas, J. J., 2014, "Dynamic and Post-Dynamic Recrystallization Under Hot, Cold and Severe Plastic Deformation Conditions," Prog. Mater. Sci., **60**(1), pp. 130–207.
[54] Su, J.-Q., Nelson, T. W., and Sterling, C. J., 2005, "Microstructure Evolution During FSW/FSP of High Strength Aluminum Alloys," Mater. Sci. Eng. A, **405**(1–2), pp. 277–286.
[55] Rhodes, C. G., Mahoney, M. W., Bingel, W. H., and Calabrese, M., 2003, "Fine-Grain Evolution in Friction-Stir Processed 7050 Aluminum," Scr. Mater., **48**(10), pp. 1451–1455.
[56] Li, D., Zhang, D., Liu, S., Shan, Z., Zhang, X., Wang, Q., and Han, S., 2016, "Dynamic Recrystallization Behavior of 7085 Aluminum Alloy During Hot Deformation," Trans. Nonferrous Met. Soc. China, **26**(6), pp. 1491–1497.
[57] Feng, X., Liu, H., and Suresh Babu, S., 2011, "Effect of Grain Size Refinement and Precipitation Reactions on Strengthening in Friction Stir Processed Al-Cu Alloys," Scr. Mater., **65**(12), pp. 1057–1060.
[58] Rokni, M. R., Zarei-Hanzaki, A., Roostaei, A. A., and Abedi, H. R., 2011, "An Investigation Into the Hot Deformation Characteristics of 7075 Aluminum Alloy," Mater. Des., **32**(4), pp. 2339–2344.
[59] Kassner, M. E., and Barrabes, S. R., 2005, "New Developments in Geometric Dynamic Recrystallization," Mater. Sci. Eng. A, **410–411**, pp. 152–155.

[60] Humphreys, F. J., and Hatherly, M., 2004, *Recrystallization and Related Annealing Phenomena*, Pergamon Press, Oxford, UK.
[61] Villumsen, M. F., and Fauerholdt, T. G., 2008, "Simulation of Metal Cutting Using Smooth Particle Hydrodynamics," LS-DYNA Anwenderforum, Bamberg, Germany, Sept. 30–Oct. 1, pp. 17–36.
[62] Tartakovsky, A., Grant, G., Sun, X., and Khaleel, M., 2006, "Modeling of Friction Stir Welding (FSW) Process With Smooth Particle Hydrodynamics (SPH)," SAE Paper No. 2006-01-1394.
[63] Patil, S., 2014, "Modeling and Characterization of Spot Weld Material Configurations for Vehicle Crash Analysis," Ph.D. thesis, Wichita State University, Wichita, KS.
[64] Agarwal, S., Briant, C. L., Hector, L. G., and Chen, Y. L., 2007, "Friction Stir Processed AA5182-O and AA6111-T4 Aluminum Alloys. Part 1: Electron Backscattered Diffraction Analysis," J. Mater. Eng. Perform., **16**(4), pp. 391–403.
[65] Özel, T., and Zeren, E., 2005, "Finite Element Method Simulation of Machining of AISI 1045 Steel With a Round Edge Cutting Tool," Eighth CIRP International Workshop on Modeling of Machining Operations, Chemnitz, Germany, May 10–11, pp. 533–542.
[66] Wang, W., Wang, K., Khan, H. A., Li, J., and Miller, S., 2018, "Numerical Analysis of Magnesium to Aluminum Joints in Friction Stir Blind Riveting," Seventh CIRP Conference on Assembly Technologies and Systems, Tianjin, China, May 10–12.
[67] Hordon, M., and Averbach, B., 1961, "X-Ray Measurements of Dislocation Density in Deformed Copper and Aluminum Single Crystals," Acta Metall., **9**(3), pp. 237–246.
[68] Williamson, G. K., and Smallman, R. E., 1955, "III. Dislocation Densities in Some Annealed and Cold-Worked Metals From Measurements on the X-Ray Debye-Scherrer Spectrum," Philos. Mag., **1**(1), pp. 34–46.
[69] Peczak, P., 1995, "A Monte Carlo Study of Influence of Deformation Temperature on Dynamic Recrystallization," Acta Metall. Mater., **43**(3), pp. 1279–1291.
[70] Mecking, H., and Kocks, U. F., 1981, "Kinetics of Flow and Strain-Hardening," Acta Metall., **29**(11), pp. 1865–1875.
[71] Kocks, U. F., 1976, "Laws for Work-Hardening and Low-Temperature Creep," ASME J. Eng. Mater. Technol., **98**(1), pp. 76–85.
[72] Estrin, Y., 1996, "Dislocation-Density-Related Constitutive Modeling," *Unified Constitutive Laws of Plastic Deformation*, A. S. Krausz and K. Krausz, eds., Academic Press, San Diego, CA, pp. 69–106.
[73] Roberts, W., and Ahlblom, B., 1978, "A Nucleation Criterion for Dynamic Recrystallization During Hot Working," Acta Metall., **26**(5), pp. 801–813.
[74] Takeuchi, S., and Argon, A. S., 1976, "Steady-State Creep of Single-Phase Crystalline Matter at High Temperature," J. Mater. Sci., **11**(8), pp. 1542–1566.
[75] Derby, B., 1991, "The Dependence of Grain Size on Stress During Dynamic Recrystallisation," Acta Metall. Mater., **39**(5), pp. 955–962.
[76] Stüwe, H. P., and Ortner, B., 1974, "Recrystallization in Hot Working and Creep," Met. Sci., **8**(1), pp. 161–167.
[77] McLean, D., 1957, *Grain Boundaries in Metals*, Oxford University Press, Oxford, UK.
[78] Peczak, P., and Luton, M. J., 1993, "A Monte Carlo Study of the Influence of Dynamic Recovery on Dynamic Recrystallization," Acta Metall. Mater., **41**(1), pp. 59–71.
[79] Read, W. T., and Shockley, W., 1950, "Dislocation Models of Crystal Grain Boundaries," Phys. Rev., **78**(3), pp. 275–289.
[80] Ding, H., Shen, N., and Shin, Y. C., 2011, "Modeling of Grain Refinement in Aluminum and Copper Subjected to Cutting," Comput. Mater. Sci., **50**(10), pp. 3016–3025.
[81] Frost, H. J., and Ashby, F., 1982, *Deformation-Mechanism Maps: The Plasticity and Creep of Metals and Ceramics*, Pergamon Press, Kidlington, UK.
[82] Woo, W., Balogh, L., Ungár, T., Choo, H., and Feng, Z., 2008, "Grain Structure and Dislocation Density Measurements in a Friction-Stir Welded Aluminum Alloy Using X-Ray Peak Profile Analysis," Mater. Sci. Eng. A, **498**(1–2), pp. 308–313.
[83] Woo, W., Ungár, T., Feng, Z., Kenik, E., and Clausen, B., 2010, "X-Ray and Neutron Diffraction Measurements of Dislocation Density and Subgrain Size in a Friction-Stir-Welded Aluminum Alloy," Metall. Mater. Trans. A, **41**(5), pp. 1210–1216.